

Research Article

One-Pot Synthesis of W-TiO₂/SiO₂ Catalysts for the Photodegradation of *p*-Nitrophenol

Ulises Arellano Sánchez ¹, Lifang Chen ², Jin An Wang ^{2,3}, Luis Enrique Noreña ³, Maximiliano Asomoza¹, Silvia Solis¹, Xiaolong Zhou ⁴, Yueqin Song⁴, and Jing Liu⁴

¹Departamento de Química, Universidad Autónoma Metropolitana-Iztapalapa, Av. San Rafael Atlixco No. 186, Iztapalapa, Mexico City, Mexico

²ESIQIE, Instituto Politécnico Nacional, Col. Zacatenco, Av. Instituto Politécnico Nacional, s/n, 07738 Mexico City, Mexico

³Departamento de Ciencias Básicas, Universidad Autónoma Metropolitana-Azcapotzalco, Av. San Pablo 180, Col. Reynosa-Tamaulipas, 02200 Mexico City, Mexico

⁴International Joint Research Center of Green Energy and Chemical Engineering, Institute of Chemical Engineering, East China University of Science & Technology, Shanghai 200237, China

Correspondence should be addressed to Lifang Chen; lchen@ipn.mx and Luis Enrique Noreña; lnf@correo.azc.uam.mx

Received 8 March 2019; Revised 30 May 2019; Accepted 17 June 2019; Published 1 August 2019

Academic Editor: Juan M. Coronado

Copyright © 2019 Ulises Arellano Sánchez et al. This is an open access article distributed under the Creative Commons Attribution License, which permits unrestricted use, distribution, and reproduction in any medium, provided the original work is properly cited.

Double modifications of TiO₂ by doping with WO₃ and by dispersing on a SiO₂ support were made by the one-pot sol-gel method. Doping with W shifts the TiO₂ band gap energy from 3.2 eV to around 3.06 eV. The surface area of the supported W-TiO₂/SiO₂ material was significantly increased, by approximately 3 times, in comparison to the bare TiO₂. The photocatalytic activities of the catalysts were evaluated in the degradation reaction of *p*-nitrophenol in aqueous solution and basic medium. After 240 min of photodegradation, more than approximately 99% *p*-nitrophenol could be mineralized with the most active W-TiO₂/SiO₂ catalyst. Under UV irradiation, *p*-nitrophenol was initially photodegraded into hydroquinone and benzosemiquinone intermediates, which were further degraded into smaller fragments such as organic carboxylic acids and finally completely mineralized. A proposed photoreaction mechanism was presented based on the key roles of the surface hydroxyl species and superoxide radicals such as O₂⁻ and ·OH, together with W⁶⁺/W⁵⁺ couples and e⁻/h⁺ pairs in the catalysts in the *p*-nitrophenol photodegradation. The one-pot sol-gel synthesis method was proven to be effective to obtain W-TiO₂/SiO₂ catalyst with large surface area and high photocatalytic activity, and it can be also used for the preparation of other heterogeneous catalysts.

1. Introduction

Industrial development around the world has greatly increased the volume of contaminated residual water [1–3]. Nanotechnology for eliminating or reducing environmental pollutants has shown significance in the last decades, particularly for water contaminant control [4]. Heterogeneous photocatalysis represents a part of the solution for addressing environmental concerns due to its significant benefits compared to traditional decontamination methods, allowing the complete mineralization of organic contaminants without producing dangerous intermediate residuals [1, 5].

Photocatalysis involves the use of solar or ultraviolet light and a semiconductor such as TiO₂ [3]. However, TiO₂ only absorbs light in the UV region due to its relatively large band gap energy (~3.2 eV), which is the main drawback for its application, since only 4~5% of the solar spectrum falls within this range [6]. The photodegradation efficiency of supported TiO₂ has improved in comparison with the bare TiO₂ solid [7, 8]. Doping TiO₂ with transition metal oxides is another effective way to overcome this problem and improve its photoactivity [9, 10].

It is known that tungsten trioxide (WO₃) is a semiconductor material with a band gap between 2.5 and 2.8 eV

[11, 12]. It is an n-type semiconductor and it may act as visible light catalyst for oxidation reactions [13]. WO_3 has several crystalline structures, depending on the synthesis conditions. The most representative tetragonal WO_3 structure forms at temperatures above 740°C ; the orthorhombic WO_3 structure can be obtained between 740 and 330°C ; the monoclinic WO_3 structure can be synthesized at a temperature interval between 330 and 17°C , and the triclinic structure can be obtained at room temperature below 17°C [14]. Due to its optical properties, WO_3 has the capacity to absorb UV and visible light from the electromagnetic spectrum [15], and thus, it has been highlighted as a photocatalyst for the photooxidation of water contaminants [16, 17]. WO_3 nanoparticles can be synthesized through the sol-gel method under different conditions [18, 19]. However, considering its high cost, small surface area, and low stability, pure WO_3 is rarely used as a catalyst but it is widely used as a photocatalyst electronic promoter or dopant. WO_3 -doped TiO_2 can reduce the band gap energy where WO_3 acts as e^- sink that would transfer photoexcited e^- to the surface grafted nanoclusters, enhancing the indoor air purification photoefficiency with visible light [20]. WO_3 -doped TiO_2 has also been reported to be active for the photodegradation of small organic compounds such as ethanol and tetracycline [21]. When WO_3 - TiO_2 was dispersed on monowalled carbon nanotubes (MWCNT), several factors responsible for the photocatalytic activity enhancement can be found in the WO_3 - TiO_2 /MWCNT nanocomposite system. Different synthesis approaches led to different crystal phase compositions thus affecting the photocatalytic activity [22].

p-Nitrophenol, widely used in industry and agriculture, has significantly contaminated water bodies, severely affecting the aquatic ecosystem. This compound has been included in the US Environmental Protection Agency list of the most toxic chemicals [23]. Meijide et al. reported that *p*-nitrophenol can be effectively degraded by the electro-Fenton process using H_2O_2 as oxidant. A kinetic model disclosing the *p*-nitrophenol photodegradation process was developed [24].

In the present work, we attempt to improve the photocatalytic activity of the TiO_2 solid by double modifications: (i) doping TiO_2 with a small amount of WO_3 in order to modify its electron structure and thus its optical properties and (ii) dispersing the W-doped TiO_2 nanoparticles onto a support, in order to increase the dispersion and the surface area. Because SiO_2 is abundant with large specific area and a good hydrothermal stability, it was chosen as the support material [25]. The TiO_2 , W- TiO_2 , and W- TiO_2 / SiO_2 solids were synthesized and later on characterized with X-ray diffraction (XRD), UV-vis spectroscopy, N_2 physisorption isotherms, X-ray photoelectron spectroscopy (XPS), scanning electron microscopy (SEM), and X-ray energy dispersion spectroscopy (EDS). Their photocatalytic activities were comparatively evaluated in the photodegradation reaction of a *p*-nitrophenol aqueous solution under basic conditions. The photoreaction mechanism and the degradation reaction pathways were explored and discussed by monitoring the reaction route.

2. Experimental

2.1. Synthesis of W- TiO_2 Nanoparticles. W- TiO_2 materials were synthesized using the sol-gel method consisting of the following stages: (1) 0.2 mol of titanium ethoxide, $\text{Ti}(\text{OC}_2\text{H}_5)_4$, and 2.4 mol of propanol were mixed; the solution was stirred over the course of 2 h. (2) 10.5 mL of a previously prepared WCl_6 /deionized solution containing 1.3 g WCl_6 was slowly added to the above solution in order to obtain 5 wt% of tungsten. The pH was adjusted to approximately 3 with 1 M HCl. (3) The mixture was kept under stirring and reflux at 70°C for 72 h in order to obtain a gel. Afterwards, the solvent was evaporated and the formed material was washed with deionized water and dried at 100°C . The material was calcined in air at 400°C for 8 h with a temperature increasing rate of $1^\circ\text{C}/\text{min}$. The obtained solid was noted as W- TiO_2 .

2.2. Synthesis of W- TiO_2 / SiO_2 . The W- TiO_2 dispersed on SiO_2 catalyst was prepared with the following stages: (1) 4 g of SiO_2 was suspended in 3.5 mol of propanol. (2) In a different container, 0.2 mol of titanium ethoxide $\text{Ti}(\text{OC}_2\text{H}_5)_4$ and 2.4 mol of propanol were mixed; the solution was stirred over the course of 2 h. (2) 10.5 mL of a previously prepared WCl_6 /deionized solution containing 1.3 g WCl_6 was slowly added to the above solution in order to obtain 5wt% W. The pH was adjusted to approximately 3 with 1 M HCl. The final molar ratio of the precursors used in the synthesis was as follows: $\text{SiO}_2 : \text{WCl}_6 : \text{Ti}(\text{OC}_2\text{H}_5)_4 : \text{C}_3\text{H}_7\text{OH} = 0.0667 : 0.0033 : 0.2 : 5.9$. (3) The mixture was kept under stirring and reflux at 70°C for 72 h to obtain a gel. After that, the solvent was evaporated and the formed material was washed with deionized water and dried at 100°C . The material was calcined in air at 400°C for 8 h with a temperature increasing rate of $1^\circ\text{C}/\text{min}$. The obtained solid was noted as W- TiO_2 / SiO_2 catalyst.

2.3. Characterization. The X-ray diffraction (XRD) patterns of the solids were obtained with a Siemens D500 diffractometer coupled to a tube with a copper anode and $\text{Cu K}\alpha$ ($\lambda = 1.5406 \text{ \AA}$) radiation. The measurements were realized at room temperature at 35 kV and 20 mA conditions. The X-ray diffraction patterns were recorded at a 2θ region between 5° and 75° .

The specific surface area, pore volume, and pore size distribution were determined with a Micromeritics ASAP 2000 instrument, using N_2 as an adsorbent. The N_2 physisorption data was converted into surface area using the Brunauer-Emmett-Teller (BET) method. The pore size distribution was calculated using the desorption isotherms according to the Barrett-Joyner-Halenda (BJH) model. Before carrying out the adsorption-desorption profile analysis, the samples were degassed in vacuum at 250°C for 4 h.

The synthesized materials were studied by diffuse reflectance UV-vis spectroscopy (DRS-UV-vis); the UV-vis spectra were obtained with a Varian Cary 100 instrument equipped with an integration sphere, using BaSO_4 as reference, at a wavelength interval from 200 to 800 nm. The UV-vis spectra were reported in diffuse reflectance mode.

The morphological features of the catalysts were studied employing a JEOL JSM-5900 LV scanning electron microscope (SEM) and a secondary emission vacuum with variable range control. The element distribution on the solid was analyzed with an energy dispersive spectrometer (EDS), model Oxford. Transmission electron microscopy (TEM) was employed in order to closely observe the dispersion of the WO_3 and TiO_2 nanoparticles on the surface of the SiO_2 solid. Micrographs were obtained with a JEM-ARM200CF microscope at an accelerating voltage of 200 kV.

The metal oxidation state and the chemical valence of the solids were determined using X-ray photoelectron spectroscopy (Thermo Scientific K-Alpha) at 150 W and 15 kV voltage. The deconvolution of the XPS peaks and curve fittings were made using the XPS Peak 4.1 software.

2.4. Photocatalytic Activity Measurement. The photocatalytic activity of the TiO_2 , W-TiO_2 , and $\text{W-TiO}_2/\text{SO}_2$ nanomaterials was evaluated in the degradation reaction of *p*-nitrophenol in an aqueous solution inside a glass photoreactor with the following steps: 200 mL of an aqueous solution containing 25 ppm of *p*-nitrophenol was poured into a container at pH 8, adjusted with a 5.0 M solution of NH_4OH , and then, 200 mg catalyst was also added. The resulting mixture was stirred inside a dark box for 30 min in order to reach adsorption-desorption equilibrium. Afterwards, a UV light source of 2.16 W (UVP Pen Ray lamp of 18 mA, 2.5 mW/cm, $\lambda \geq 365$ nm) was used to irradiate the photoreactor.

At regular intervals of 30 min of irradiation, aliquots of 3 mL were taken, which were filtered (0.45 microns nylon filters) in order to eliminate suspended solid particles. The *p*-nitrophenol photodegradation was determined by measuring the characteristic absorption peak that appears at approximately 400 nm using UV-vis spectrophotometry (Varian Cary 100 UV-vis). Formation of different intermediates was monitored by liquid chromatography-mass spectrometry (LC-MS) on time analysis in order to explore the possible degradation mechanisms or pathways.

The catalytic stability test was carried out 5 successive times under the same reaction conditions reported above. After the end of each experiment, the catalyst was filtered and dried without calcination, and then, it was used for the next test.

3. Results and Discussion

3.1. X-Ray Diffraction. Figure 1 shows the XRD patterns of the TiO_2 , W-TiO_2 , and $\text{W-TiO}_2/\text{SiO}_2$ catalysts. For the pure TiO_2 sample, the diffractograms show several peaks at $2\theta = 25.3, 37.5, 48.0, 53.8, 55.9,$ and 63.5° which correspond to the reflections of the (101), (004), (200), (105), (211), and (204) planes in the crystalline anatase TiO_2 (JCPDS 21-1272). For the W-TiO_2 solid, several diffraction peaks appear at $2\theta = 23.2, 23.6, 28.6, 33.3, 33.7,$ and 41.5° which correspond to the reflections of the (001), (200), (111), (021), (201), and (221) planes of the monoclinic WO_3 [26, 27]. For the $\text{W-TiO}_2/\text{SiO}_2$ sample, the peaks became broader and weaker. The XRD peaks of WO_3 are slightly wide, which is attributed to the high dispersion of W-TiO_2 , since the

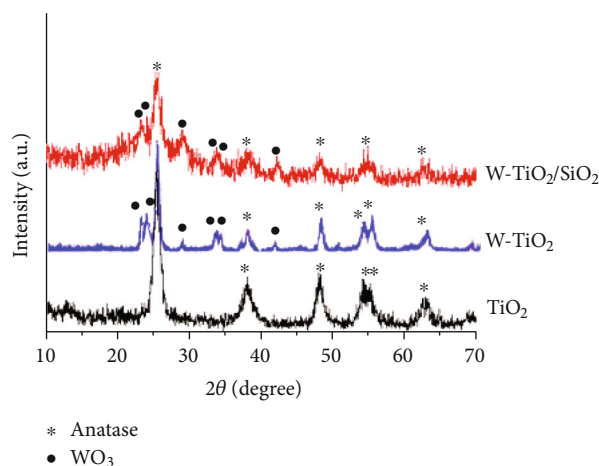


FIGURE 1: X-ray diffraction patterns of TiO_2 , W-TiO_2 , and $\text{W-TiO}_2/\text{SiO}_2$ catalysts.

content of W is rather low (approximately 5 wt% in TiO_2) in the nanomaterial [28, 29].

3.2. UV-vis Diffuse Reflectance Spectroscopy (DRS-UV-vis). Figure 2 shows the DRS-UV-vis spectra of the TiO_2 , W-TiO_2 , and $\text{W-TiO}_2/\text{SiO}_2$ solids. The values of the band gap energy (E_g) were calculated using the Tauc method [30], which consists of graphing the $h\nu$ product (light energy) on the x -axis and the $(\alpha h\nu)^{1/r}$ on the ordinate, where α is the absorption coefficient of the material. The E_g values of TiO_2 , W-TiO_2 , and $\text{W-TiO}_2/\text{SiO}_2$ are reported in Table 1. After W doping, the E_g value diminishes from 3.2 eV for TiO_2 to around 3.06 eV for W-TiO_2 and $\text{W-TiO}_2/\text{SiO}_2$. Relative to pure TiO_2 , the UV-vis spectrum of the W-TiO_2 catalyst presents a small displacement towards the visible electromagnetic region. This probably resulted from the electronic interaction within the WO_3 and TiO_2 material heterojunction [31]. The UV-vis spectrum of the $\text{W-TiO}_2/\text{SiO}_2$ solid exhibited an absorption profile similar to W-TiO_2 . This behavior is attributed to the fact that SiO_2 is transparent to the UV-vis radiation [32].

3.3. N_2 Adsorption-Desorption Isotherms. The textural properties of the TiO_2 , W-TiO_2 , and $\text{W-TiO}_2/\text{SiO}_2$ samples were measured. Table 1 shows the specific surface area (BET), pore volume, and average pore diameter of TiO_2 , W-TiO_2 , and $\text{W-TiO}_2/\text{SiO}_2$. TiO_2 and W-doped TiO_2 solids present a surface area of 140 and $126 \text{ m}^2/\text{g}$, respectively. W doping leads to a slight reduction of surface area probably due to the partial blockage of some pores by WO_x deposits. After loading the sol-gel W-TiO_2 nanoparticles on the SiO_2 support, the surface area significantly increases to $432 \text{ m}^2/\text{g}$. Therefore, the supported W-TiO_2 solids show greater dispersion and much higher surface area in comparison with the unsupported W-TiO_2 solids, probably as a result from the strong mutual interaction between hydroxyls in W-TiO_2 and SiO_2 , preventing rapid crystallization and particle growth. The stretching out hydroxyls in the SiO_2 support may highly connect with the $-\text{OH}$ species in $\text{Ti}(\text{OH})_4$ and

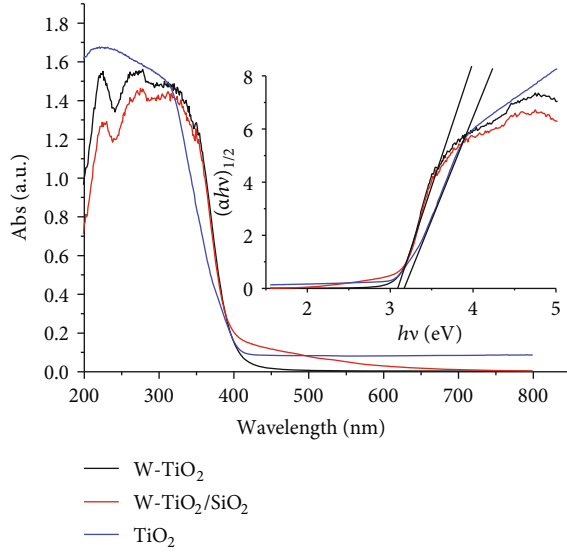


FIGURE 2: DRS-UV-vis spectra and Kubelka-Munk function versus energy ($h\nu$) plots for the TiO_2 , W-TiO_2 , and $\text{W-TiO}_2/\text{SiO}_2$ catalysts.

TABLE 1: Textural data and E_g values of TiO_2 , W-TiO_2 , and $\text{W-TiO}_2/\text{SiO}_2$ *.

Samples	S_{BET} (m^2/g)	D_p (\AA)	V_p (cm^3/g)	E_g (eV)
TiO_2	140	39	0.21	3.20
W-TiO_2	126	38	0.20	3.06
$\text{W-TiO}_2/\text{SiO}_2$	432	29	0.21	3.06

* S_{BET} : surface area obtained by BET method; D_p : average pore size; V_p : pore volume; E_g : gap band energy.

W(OH)_6 produced by the hydrolysis of the titanium and tungsten precursors during the synthesis, gaining the dispersion of the W-TiO_2 nanoparticles formed on the SiO_2 solid after calcination.

3.4. Morphological Features and Element Distribution. Figure 3 shows SEM micrographs and the Si, Ti, and O chemical composition distribution of the TiO_2 , W-TiO_2 , and $\text{W-TiO}_2/\text{SiO}_2$ solids. For the TiO_2 sample, on the selected area only Ti and O elements were detectable by EDS. For the W-TiO_2 solid, W, Ti, and O on the surface of TiO_2 were observed on the selected area. For the $\text{W-TiO}_2/\text{SiO}_2$ sample, Si, Ti, W, and O distribution was confirmed. Elementary carbon may result from the titanium ethoxide $\text{Ti(OC}_2\text{H}_5)_4$ or tetraethylorthosilicate (TEOS) precursors during the synthesis.

More information on the element distribution along the whole samples was investigated with the EDS mapping technique. Figure 4 shows the EDS mappings of TiO_2 and W-TiO_2 samples. A very uniform distribution of O and Ti elements in the pure TiO_2 was observed. In the W-doped TiO_2 sample, we may see that W was homogeneously distributed across the whole TiO_2 particles.

For a closer observation of the distribution of WO_3 and TiO_2 nanoparticles on the SiO_2 surface, the transmission electron microscopy technique was employed. Figure 5 shows the TEM images of W-TiO_2 and $\text{W-TiO}_2/\text{SiO}_2$ samples. On the W-TiO_2 sample (Figure 5(a)), both WO_3 and TiO_2 nanoparticles are observed. Their particle sizes ranged between 5 and 20 nm. Some WO_3 and TiO_2 particles contacted each other, forming W-TiO_2 mixed oxides. Some crystal terrace and kinks in TiO_2 crystals are observed. In Figure 5(b), we observe WO_3 and TiO_2 particles highly dispersed on the surface of the SiO_2 solid. Some large TiO_2 anatase phases were surrounded with WO_3 small particles. The particle size of TiO_2 varied between 5 and 20 nm whereas WO_3 particles are relatively small, most ranging from 4 to 10 nm. The TEM observations are consistent with XRD results, where wide XRD peaks corresponding to monoclinic WO_3 and anatase TiO_2 phase are present in both W-TiO_2 and $\text{W-TiO}_2/\text{SiO}_2$ samples.

3.5. X-Ray Photoelectron Spectroscopy (XPS) Analysis. Figure 6 shows the XPS spectra of the TiO_2 , W-TiO_2 , and $\text{W-TiO}_2/\text{SiO}_2$ catalysts. In Figure 6(a), the core levels of O 1s XPS spectra can be deconvoluted into two parts: the large peak with binding energy (BE) between 528.0 and 531.4 eV corresponds to the lattice oxygen in oxides; the small peaks with a BE value of 531.5~534.0 eV indicate the surface oxygen species such as hydroxyls and adsorbed water [33]. The Ti2p core levels of the XPS spectra are shown in Figure 6(b). Two well-defined peaks are clearly present, and they correspond to the Ti2p1/2 (BE = 462~456 eV) and Ti2p3/2 (BE = 456~460 eV) signals, confirming the Ti^{4+} ion in anatase phase [34]. When TiO_2 was doped with W, the peak positions slightly shifted towards the high-energy region; when the W-TiO_2 solid was dispersed on the SiO_2 surface, this shift became more significant. Considering that the cationic size of W^{6+} (0.62 \AA) is slightly smaller than that of Ti^{4+} (0.69 \AA), during the synthesis procedure, W ions may insert into the Ti lattice points resulting in the W-O-Ti bond. These peak shifts may indicate both, the formation of the W-O-Ti bond in the structure and the interaction between W-TiO_2 and the SiO_2 support.

The W4f core levels of the XPS spectra are present in Figure 6(c). Each of them can be deconvoluted into two peaks, indicating the coexistence of W^{6+} (BE = 35.1~35.5 eV for W4f 7/2 and BE = 37.5~38.2 eV for W4f 5/2) and W^{5+} (BE = 34.2~34.4 eV for W4f 7/2 and BE = 36.8~37.0 eV for W4f 5/2) [35, 36]. The Si2p core level of the XPS spectrum, Figure 6(d), shows only one symmetrical peak at 101~106 eV [37]. The XPS characterization confirms that a certain number of hydroxyl species, surface-adsorbed oxygen species, lattice oxygen, and $\text{W}^{6+}/\text{W}^{5+}$ ions coexist in the W-doped TiO_2 solids.

The surface atomic concentrations of the samples obtained from the XPS analysis are reported in Table 2. For the $\text{W-TiO}_2/\text{SiO}_2$ catalyst, the surface oxygen concentration is greater than that for both TiO_2 and W-TiO_2 materials. This is probably due to more hydroxyls present on the surface of the solid. Some of them result from the SiO_2 support. These surface oxygen species are the precursors of active

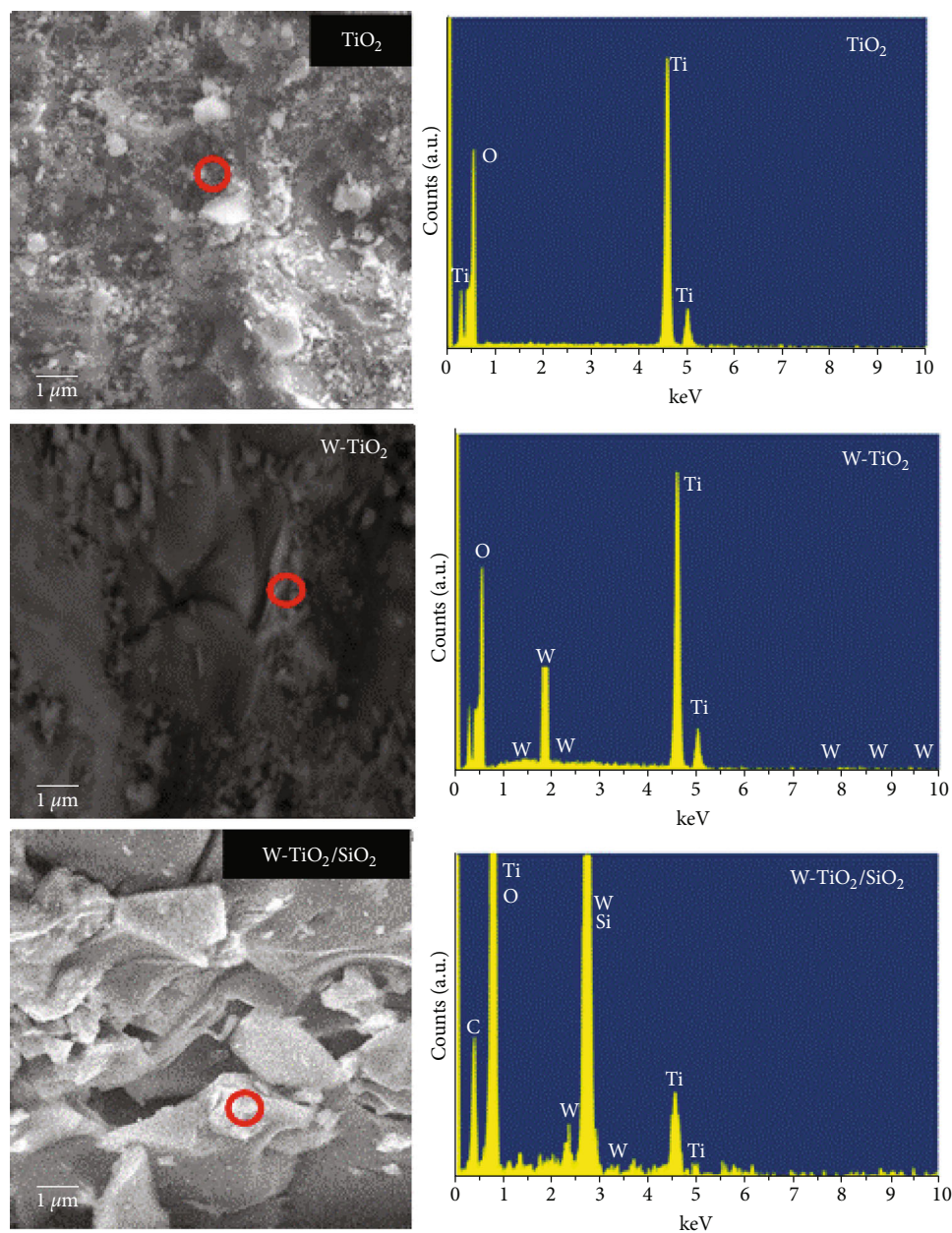


FIGURE 3: SEM micrographs and EDS profiles of selected areas on the TiO_2 , W-TiO_2 , and $\text{W-TiO}_2/\text{SiO}_2$ catalysts.

oxygen species such as $\cdot\text{OH}$ or $\text{O}_2\cdot^-$ radicals. The presence of more surface active oxygen species may increase the photocatalytic activity.

3.6. Photocatalytic Activity. Usually, *p*-nitrophenol may exist in two forms in aqueous solution, depending on the pH value. Figure 7 shows the UV-vis absorption bands of *p*-nitrophenol at pH = 6. Two bands at 220 nm and 399 nm are shown, corresponding to the *p*-nitrophenol protonated form and to the nonprotonated *p*-nitrophenol ion form, respectively. The former usually appears in acidic conditions and the latter can be formed under basic conditions. In the present experiments, the *p*-nitrophenol photodegradation reaction was initially performed at pH = 8. Therefore, only

the intensity variation of the band corresponding to the nonprotonated *p*-nitrophenol was monitored during the whole reaction procedure.

Figure 8 shows the absorption spectra of *p*-nitrophenol in function of the UV irradiation time for the most active catalyst, $\text{W-TiO}_2/\text{SiO}_2$. During the degradation, the intensity of the absorption band gradually diminishes as the pH value gradually increases from the initial pH = 8 to 10 at the end of a 240 min reaction. The pH value variation must be related to the products formed during the degradation, relationship which will be further discussed below.

Figure 9 shows the remaining concentration of *p*-nitrophenol after photodegradation with the TiO_2 , W-TiO_2 , and $\text{W-TiO}_2/\text{SiO}_2$ catalysts under UV irradiation. In the initial

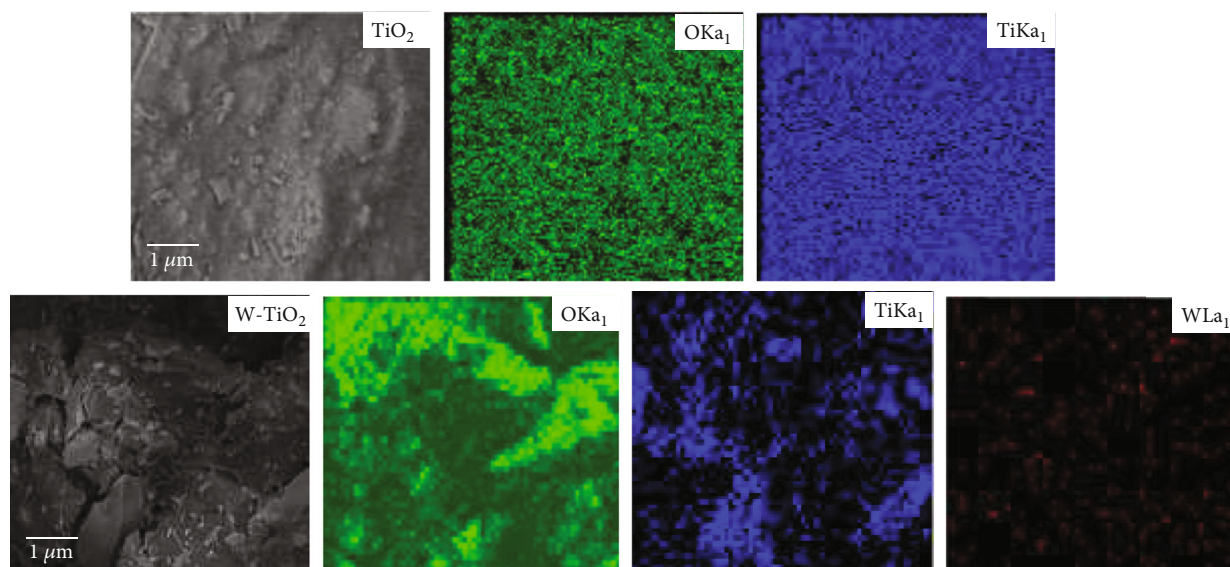


FIGURE 4: Element distribution mappings for the TiO_2 and the W-TiO_2 dispersed on the SiO_2 solid.

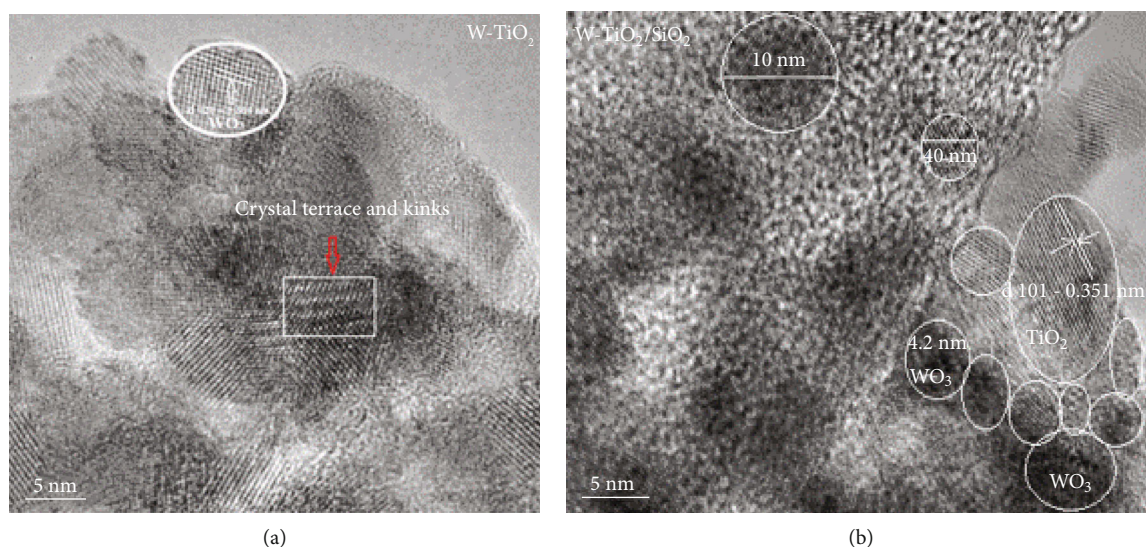


FIGURE 5: TEM micrographs of the W-TiO_2 (a) and $\text{W-TiO}_2/\text{SiO}_2$ (b) catalyst solids.

adsorption period (15 min), the *p*-nitrophenol concentration was reduced from 25 ppm to 24.6 ppm for TiO_2 , to 24.4 ppm for W-TiO_2 , and to 22.8 ppm for the $\text{W-TiO}_2/\text{SiO}_2$ catalyst. These results indicate that the *p*-nitrophenol adsorption ability of $\text{W-TiO}_2/\text{SiO}_2$ is greater in comparison to TiO_2 and W-TiO_2 . This can be principally attributed to the greater specific area of $\text{W-TiO}_2/\text{SiO}_2$.

After 240 min of irradiation, the concentration of *p*-nitrophenol significantly diminishes to 13.2 ppm employing TiO_2 ; thereafter, only 52.8% of *p*-nitrophenol was converted; so the activity of pure TiO_2 for *p*-nitrophenol degradation is relatively low. A better activity was achieved using the W-TiO_2 catalyst since the *p*-nitrophenol conversion reached 88.2% at the end of reaction. The $\text{W-TiO}_2/\text{SiO}_2$ catalyst

exhibits the greatest activity, leaving a remnant of 2.6 ppm of *p*-nitrophenol at 180 min of reaction. After 240 min, approximately 99% *p*-nitrophenol was photocatalytically degraded, reaching almost complete removal.

The stability of three catalysts was evaluated. The results are presented in Figure 10. The catalytic test was repeated 4 times under the same reaction conditions. At the end of each experiment, the catalysts were filtered and dried and then used in the next test. We found that the TiO_2 catalyst could remove around 50-53% of *p*-nitrophenol in four successive recycles. In the first cycle, approximately 80% and 99% of *p*-nitrophenol could be degraded by the W-TiO_2 and $\text{W-TiO}_2/\text{SiO}_2$ catalysts, respectively. The degradation of *p*-nitrophenol gradually diminished in

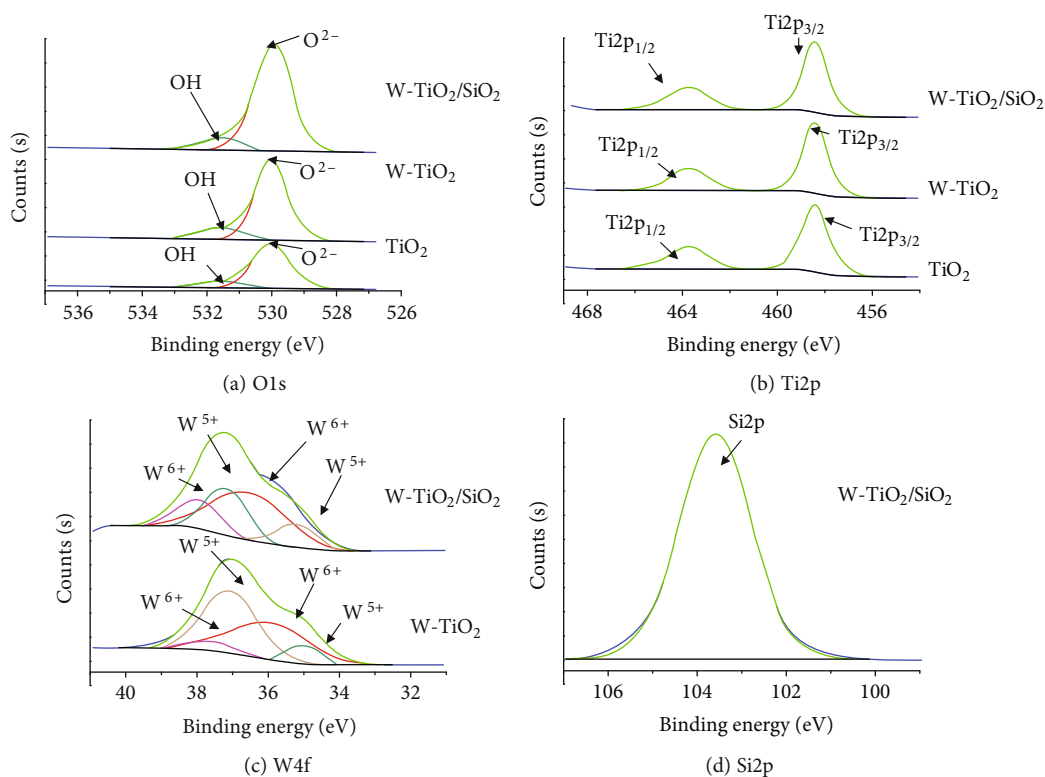


FIGURE 6: XPS spectra of the TiO_2 , W-TiO_2 , and $\text{W-TiO}_2/\text{SiO}_2$ samples.

TABLE 2: Surface atomic concentration (wt%) obtained from XPS analysis.

Catalyst samples	Surface atomic concentration (wt%)			
	Ti2p	O1s	Si2p	W4f
TiO_2	60.67	39.33		
W-TiO_2	56.89	40.01		3.10
$\text{W-TiO}_2/\text{SiO}_2$	28.53	46.57	26.91	1.80

the following trials. In the fourth cycle, an approximately 15-20% drop of the catalytic activity was observed that may result from the catalyst mass loss during the filtration procedure. In the fifth cycle, we added a little amount of fresh catalysts for compensating the catalyst loss and keep the catalyst mass unchanged. Then, we found that the *p*-nitrophenol photodegradation rate became very similar to the results obtained in the first cycle, confirming that the decrease in catalytic activity was caused by the catalyst mass loss in the operation procedure.

4. Discussion

In this work, we dispersed W-TiO_2 nanoparticles on SiO_2 solids by the sol-gel method. SiO_2 may take two roles: (1) it provides a larger surface area for better dispersing the W-TiO_2 active phases, as confirmed by the significant

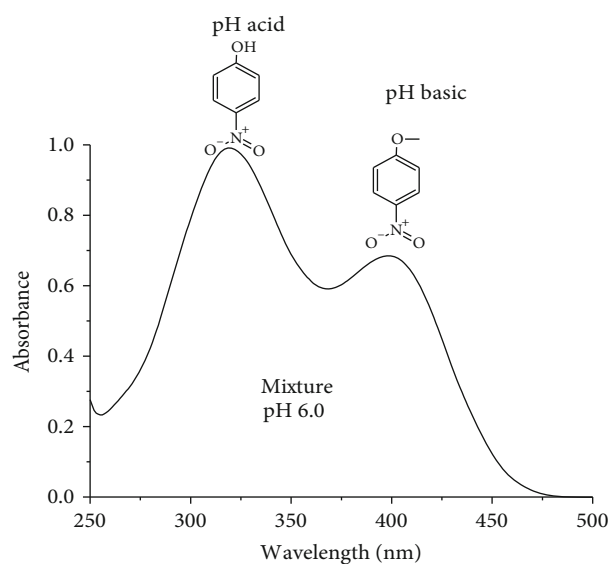


FIGURE 7: UV-vis spectrum of *p*-nitrophenol aqueous solution at pH 6.

increase of approximately 3 times, of the surface area in comparison to that of bare TiO_2 , and approximately 3.5 times relative to W-TiO_2 (see Table 1); and (2) SiO_2 also provides additional surface hydroxyls that participate in the formation of $\cdot\text{OH}$ radicals under UV irradiation.

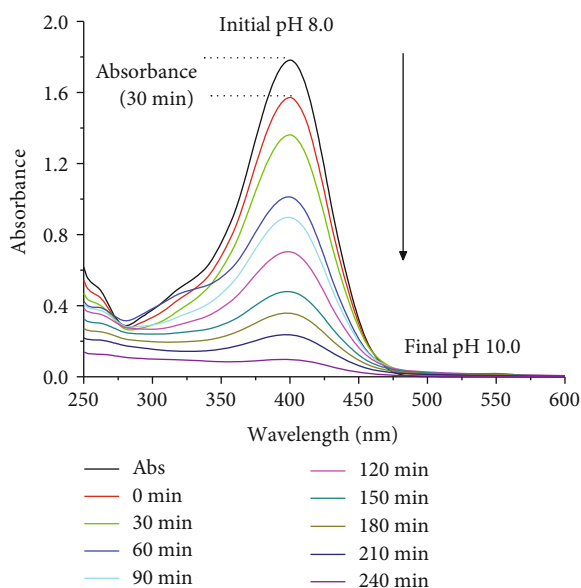
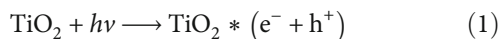


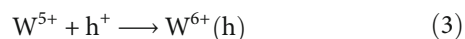
FIGURE 8: A set of UV-vis spectra of *p*-nitrophenol aqueous solution recorded at various degradation times in the presence of the W-TiO₂/SiO₂ catalyst. The pH value of the solution varied from an initial pH = 8 to pH = 10 after 240 min of reaction.

The XPS characterization confirms that in W⁶⁺ and W⁵⁺ ions, a certain number of hydroxyl species and surface oxygen species coexist in the W-TiO₂ and W-TiO₂/SiO₂ catalysts. Therefore, some W⁶⁺/W⁵⁺ couples are formed in these catalysts even before the photoreactions. The formation of W⁵⁺ may result from W⁶⁺ accepting an electron transferring from surface OH species; and it may also indicate the existence of some oxygen defects around W⁶⁺ in the crystalline structure of WO₃ nanocrystals. During the W-TiO₂ synthesis, some W⁶⁺ ions can replace some of the Ti⁴⁺ ions in the TiO₂ lattices in order to form a W-O-Ti bond. However, because W⁶⁺ (0.62 Å) has a smaller ion radius than Ti⁴⁺ (0.69 Å), the W-O-Ti bond formation may lead to an unbalance of the local electron cloud distribution that results in a more active local oxygen, favoring the surface oxidation reaction.

It is widely recognized that there are some electron (e⁻)-hole (h⁺) pairs in the surface of the activated TiO₂* induced by UV irradiation



In the W-doped TiO₂ catalyst under UV irradiation, the charge transfer cycles in the W⁶⁺/W⁵⁺ couples may occur *via* W⁶⁺ capturing an electron and converting to W⁵⁺ (equation (2)) or *via* W⁵⁺ hole (h⁺) trapping and converting to W⁶⁺ (equation (3)):



Therefore, the coexistence of W⁶⁺/W⁵⁺ couples, (e⁻)-(h⁺) pairs, and surface oxygen species such as hydroxyls may promote the surface reduction-oxidation cycles.

It has been reported that a heterojunction structure can be formed in the interfaces of the dopant and parent semiconductor nanoparticles [38]. When such a heterojunction is initiated by photons with energy higher than or equal to the bandgap of the semiconductor, herein, W-TiO₂, the photoinitiated electron-hole pairs can be quickly separated: the electrons in the TiO₂ conduction band (CB) may flow to the WO₃ nanoparticles CB because the TiO₂ CB is more negative than that of WO₃. Simultaneously, the valence bands (VB) of WO₃ and TiO₂ oxides are mainly constituted by their O2p orbital, and therefore, their VB energy levels are rather close. Considering the charge balance in the semiconductor, the photoexcited holes in the VB would more likely transfer from WO₃ to TiO₂ [38]. Such charge transferring effectively inhibits the recombination rate of electron-hole pairs. Electron and hole migration driven by the electron field force within the heterojunction further promotes the reduction-oxidation cycles of the W⁶⁺/W⁵⁺ couple in the W-TiO₂/SiO₂ catalyst.

In the present experiment, the photodegradation of *p*-nitrophenol was performed in the presence of air. Under the oxidation reaction condition and the UV irradiation, surface W⁵⁺ ions can be oxidized to W⁶⁺ ions via W⁵⁺ transferring an electron to the molecular O₂ adsorbed on the surface of the TiO₂ particle, forming O₂⁻ (equation (4)); on the other hand, the accumulated electrons in WO₃ can be consumed by reducing W⁶⁺ ions to W⁵⁺ ions via interacting with surface hydroxyl (OH⁻) species which liberate an electron and convert OH⁻ into ·OH radicals (equation (5)).



Therefore, in the *p*-nitrophenol photodegradation process, an oxidation half cycle (equations (3) and (4)) and a reduction half cycle (equations (2) and (5)) coexist, accompanied by electrons transfer from the hydroxyls to the ·OH radicals, and from O₂ to O₂⁻, among the electron (e⁻)-hole (h⁺) pairs and W⁶⁺/W⁵⁺ couples in the catalyst surface. These ·OH and O₂⁻ radicals are the principal active species for the photodegradation of *p*-nitrophenol. A photodegradation reaction mechanism involving the oxidation-reduction cycles taking place on the surface of the W-TiO₂/SiO₂ catalyst is proposed in Scheme 1.

When the *p*-nitrophenol photodegradation was catalyzed with the W-TiO₂/SiO₂ catalyst, various intermediates were formed involving several reaction steps. At the beginning of the degradation stage under UV irradiation, the stretching -NO₂ and -OH groups interacted with the catalyst and were easily attacked by surface active oxygen species such as superoxide radicals O₂⁻ and ·OH, leading to the formation of the primary intermediate fragments such as 2,4-benzoquinone, *p*-benzoquinone, and 4-nitrocatechol.

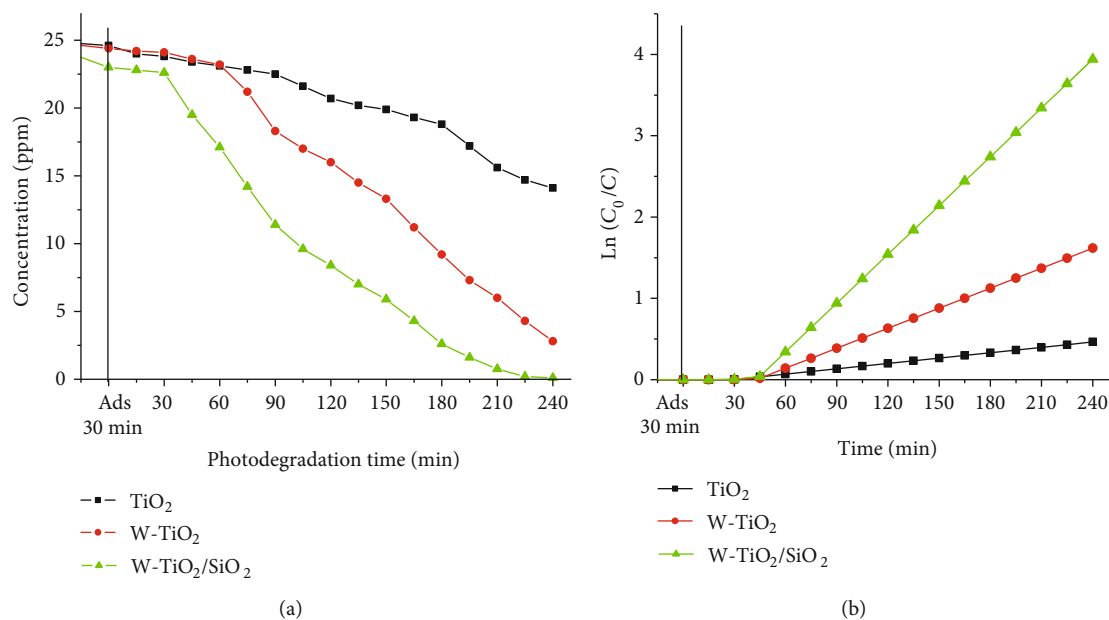


FIGURE 9: (a) Plots of *p*-nitrophenol concentration as a function of irradiation time in the presence of TiO₂, W-TiO₂, and W-TiO₂/SiO₂ catalysts; (b) plots of $\ln(C_0/C)$ as a function of reaction time.

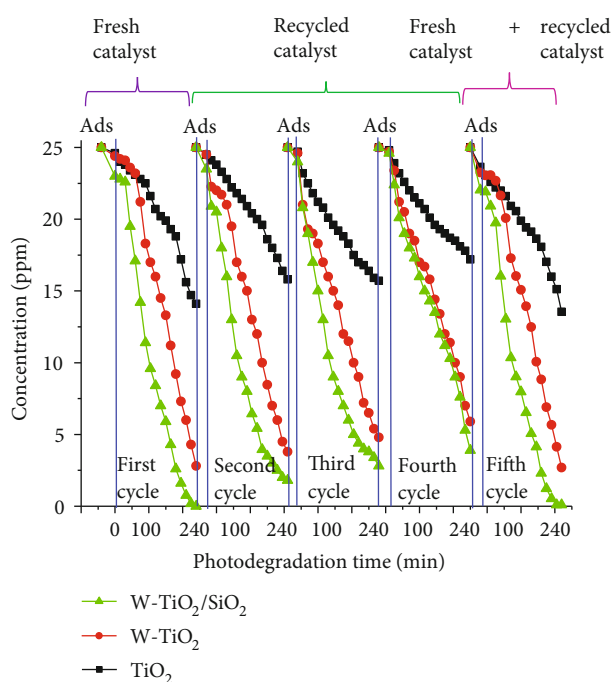
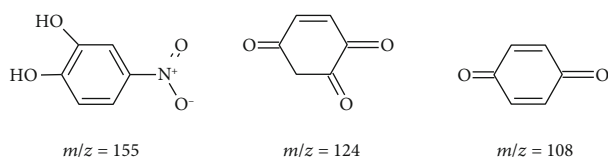


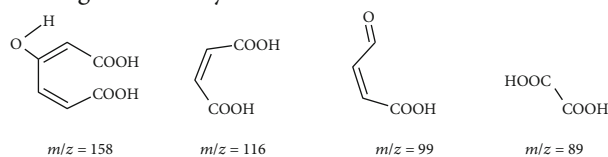
FIGURE 10: Reusability test of the TiO₂, Ti-TiO₂, and W-TiO₂/SiO₂ catalysts.



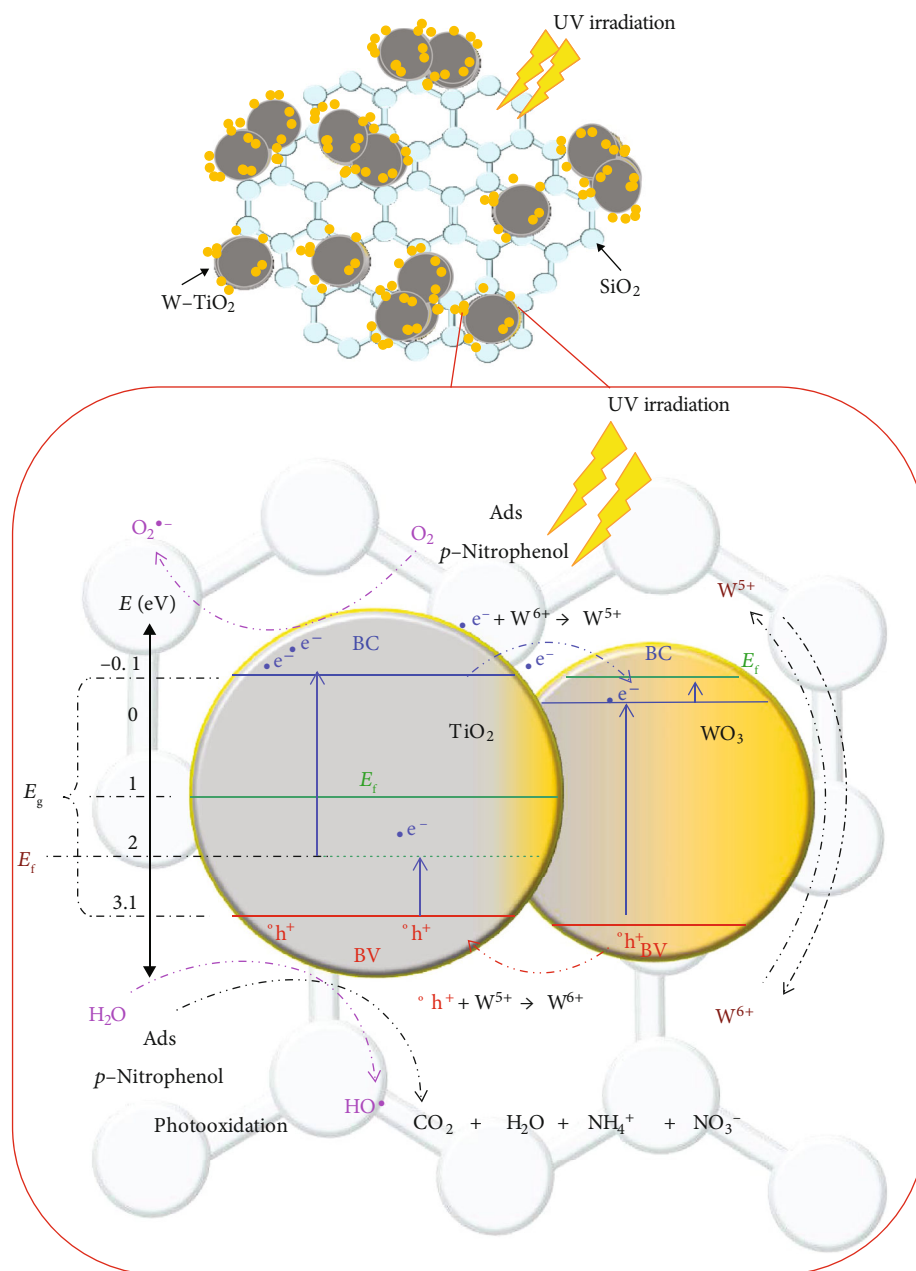
The formation of the primary intermediate fragments is related to the special molecular structure of *p*-nitrophenol.

Collado et al. reported that there is an electron withdrawing effect of the *p*-hydroxybenzoic acid [39]. In this work, the -NO₂ group in the *p*-nitrophenol structure may generate an electron withdrawing effect in the *para* position of the aromatic ring, which influences the hydroxyl group and thus inhibits the rate of the electrophilic attack reaction for the formation of catechol and hydroquinone. As a result, 2,4-benzoquinone, *p*-benzoquinone, and 4-nitrocatechol are chiefly formed at the initial stage. Because the -NO₂ group is a leaving group which can be eliminated easily, *p*-nitrophenol could form the hydroquinone and benzosemiquinone intermediates via the rupture of the C-N bond [40].

As the reaction further proceeded, the formed benzoquinones and nitrocatechol species gradually disappeared, and instead, 3-hydroxymuconic acid and other organic acids (acetic acid, oxalic acid, and maleic acid) were detectable. These results indicate that the primary fragments were further degraded into secondary species with a smaller molecular mass through the cleavage of C-C bonds by cycloaddition reactions, leading to the aromatic ring opening followed by the formation of secondary fragments such as various organic carboxylic acids.



After 4 hours of photocatalytic reaction, the secondary intermediates were further degraded into species with smaller molecular masses and finally mineralized into CO₂ and NH₄⁺ and water. The pH value increased from 8 to 10 during the reaction, indicating that the intermediates with small molecules or short-chain acids formed in the last step were finally degraded into CO₂ and water. Formation of



SCHEME 1: A proposed photoreaction mechanism and charge transfer on the surface of the W-TiO₂/SiO₂ catalyst.

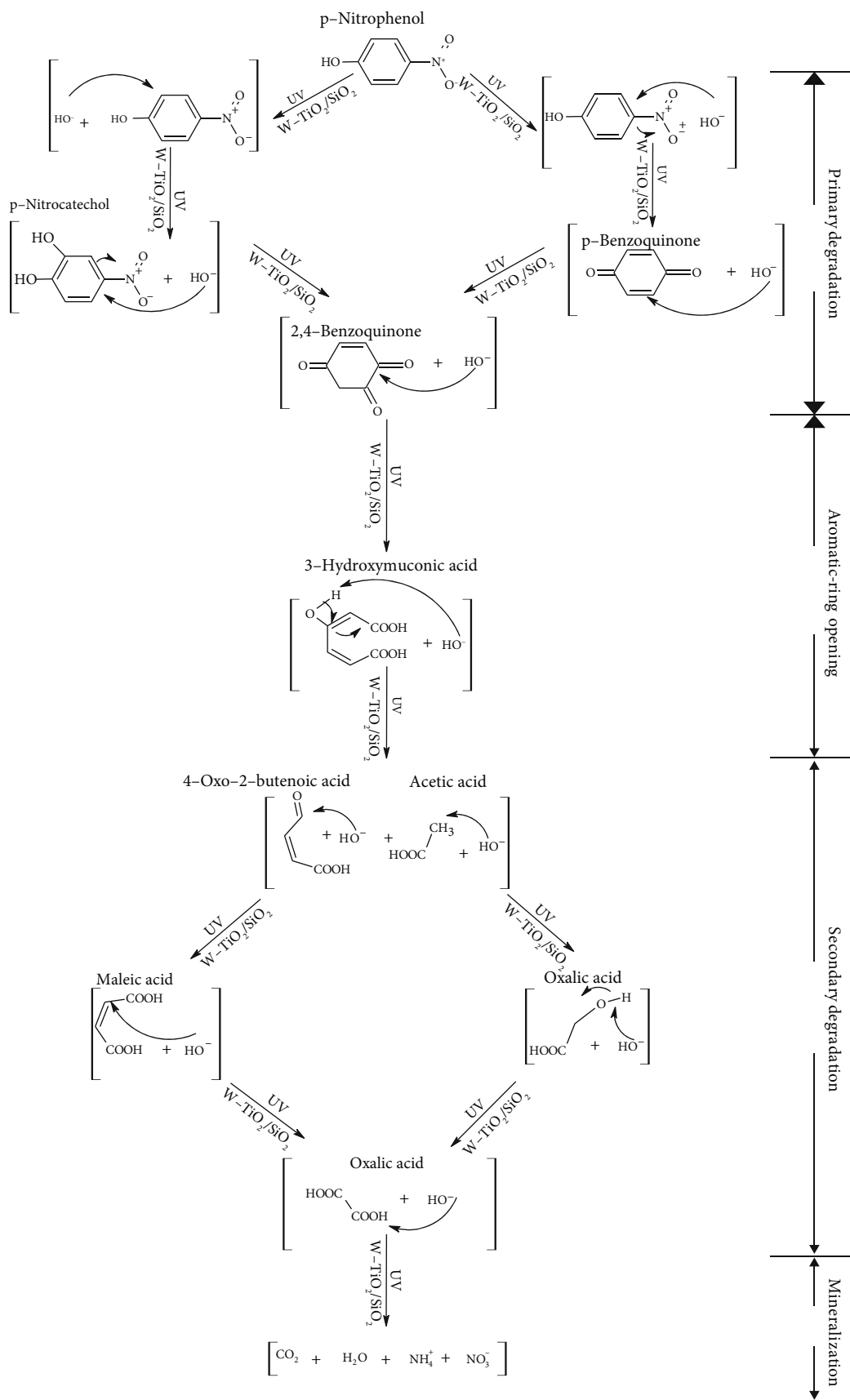
additional OH⁻ species in the solution may lead to the pH increment. These results suggest the complete mineralization of *p*-nitrophenol. The possible reaction pathways are pictured in Scheme 2.

5. Conclusions

The one-pot sol-gel synthesis method reported herein was proven to be effective to obtain a W-TiO₂/SiO₂ catalyst with a large surface area and high photocatalytic activity, and it can be also used for the preparation of other heterogeneous catalysts. The XPS and UV-vis spectra show that after W doping, a slight displacement of the electromagnetic

spectrum towards the visible region was observed for the W-TiO₂ catalyst. When the W-TiO₂ nanoparticles were dispersed on SiO₂, their surface area was greatly increased by approximately 3 times. The synthesis conditions reported herein favor the formation of the crystalline titania anatase phase and enhance the dispersion of W-TiO₂ nanoparticles with high dispersion and a large surface area.

In the photodegradation reaction of *p*-nitrophenol in basic conditions under UV irradiation and after 4 h reaction, the most active W-TiO₂/SiO₂ catalyst degraded more than 99% of *p*-nitrophenol. The activity of the catalyst has been attributed to the high dispersion of W-TiO₂ within the silica matrix with the greater surface area and to the formation of a

SCHEME 2: Pathways of the *p*-nitrophenol photodegradation reaction under UV irradiation in the presence of the catalyst.

heterojunction at the interface between WO_3 and TiO_2 . The surface hydroxyls and superoxide radicals such as O_2^- and $\cdot\text{OH}$, together with $\text{W}^{6+}/\text{W}^{5+}$ reduction-oxidation couples and e^- - h^+ pairs, took key roles in the complete mineralization of *p*-nitrophenol.

Data Availability

The data used to support the findings of this work are available from the corresponding authors upon request.

Conflicts of Interest

The authors declare herein that this article currently has no conflict of interests.

Acknowledgments

We would like to thank the financial support from the projects of Instituto Politécnico Nacional (SIP-20181280 and SIP-20180199) and an international scientific collaboration between the International Joint Research Centre of Clean Energy and Chemical Engineering at the East China University of Science and Technology and the Instituto Politécnico Nacional in Mexico. J.A. Wang thanks the Departamento de Ciencias Básicas, Universidad Autónoma Metropolitana-Azcapotzalco for supporting his investigation during his Sabbatical year.

References

- [1] M. J. López-Muñoz, J. Aguado, and A. Revilla, "Photocatalytic removal of s-triazines: evaluation of operational parameters," *Catalysis Today*, vol. 161, no. 1, pp. 153–162, 2011.
- [2] N. Miranda-García, S. Suárez, M. I. Maldonado, S. Malato, and B. Sánchez, "Regeneration approaches for TiO_2 immobilized photocatalyst used in the elimination of emerging contaminants in water," *Catalysis Today*, vol. 230, pp. 27–34, 2014.
- [3] J. A. Navio, F. J. Marchena, C. Cerrillos, and F. Pablos, "UV photolytic degradation of butyltin chlorides in water," *Journal of Photochemistry and Photobiology A: Chemistry*, vol. 71, no. 1, pp. 97–102, 1993.
- [4] S. Malato, P. Fernández-Ibáñez, M. I. Maldonado, J. Blanco, and W. Gernjak, "Decontamination and disinfection of water by solar photocatalysis: recent overview and trends," *Catalysis Today*, vol. 147, no. 1, pp. 1–59, 2009.
- [5] S. Murgolo, F. Petronella, R. Ciannarella et al., "UV and solar-based photocatalytic degradation of organic pollutants by nano-sized TiO_2 grown on carbon nanotubes," *Catalysis Today*, vol. 240, pp. 114–124, 2015.
- [6] W. Dai, X. Wang, P. Liu, Y. Xu, G. Li, and X. Fu, "Effects of electron transfer between TiO_2 films and conducting substrates on the photocatalytic oxidation of organic pollutants," *The Journal of Physical Chemistry B*, vol. 110, no. 27, pp. 13470–13476, 2006.
- [7] S. Banerjee, S. K. Mohapatra, P. P. Das, and M. Misra, "Synthesis of coupled semiconductor by filling 1D TiO_2 nanotubes with CdS ," *Chemistry of Materials*, vol. 20, no. 21, pp. 6784–6791, 2008.
- [8] Y. Xu and C. H. Langford, "Enhanced photoactivity of a titanium(IV) oxide supported on ZSM5 and zeolite A at low coverage," *The Journal of Physical Chemistry*, vol. 99, no. 29, pp. 11501–11507, 1995.
- [9] P. Pichat, *Photocatalysis and Water Purification: From Fundamentals to Recent Applications*, G. Q. M. Lu, Ed., Wiley-VCH, Germany, 2013.
- [10] L. E. Noreña and J.-A. Wang, *Advanced Catalytic Materials - Photocatalysis and Other Current Trends*, Published by INTECH Publications Ltd., 2016.
- [11] G. R. Bamwenda and H. Arakawa, "The visible light induced photocatalytic activity of tungsten trioxide powders," *Applied Catalysis A: General*, vol. 210, no. 1–2, pp. 181–191, 2001.
- [12] S. J. Hong, H. Jun, P. H. Borse, and J. S. Lee, "Size effects of WO_3 nanocrystals for photooxidation of water in particulate suspension and photoelectrochemical film systems," *International Journal of Hydrogen Energy*, vol. 34, no. 8, pp. 3234–3242, 2009.
- [13] X. Wang, G. Liu, Z. G. Chen et al., "Enhanced photocatalytic hydrogen evolution by prolonging the lifetime of carriers in ZnO/CdS heterostructures," *Chemical Communications*, vol. 23, no. 23, pp. 3452–3454, 2009.
- [14] E. Ozkan Zayim, P. Liu, S.-H. Lee et al., "Mesoporous sol-gel WO_3 thin films via poly(styrene-co-allyl-alcohol) copolymer templates," *Solid State Ionics*, vol. 165, no. 1–4, pp. 65–72, 2003.
- [15] T. Todorovski and M. Najdoski, "The solution growth route and characterization of electrochromic tungsten oxide thin films," *Materials Research Bulletin*, vol. 42, no. 12, pp. 2025–2031, 2007.
- [16] Z. G. Zhao and M. Miyauchi, "Shape modulation of tungstic acid and tungsten oxide hollow structures," *The Journal of Physical Chemistry C*, vol. 113, no. 16, pp. 6539–6546, 2009.
- [17] A. Enesca, A. Duta, and J. Schoonman, "Study of photoactivity of tungsten trioxide (WO_3) for water splitting," *Thin Solid Films*, vol. 515, no. 16, pp. 6371–6374, 2007.
- [18] K. Nishio and T. Tsuchiya, "Electrochromic thin films prepared by sol-gel process," *Solar Energy Materials & Solar Cells*, vol. 68, no. 3–4, pp. 279–293, 2001.
- [19] W. Wang, Y. Pang, and S. N. B. Hodgson, "XRD studies of thermally stable mesoporous tungsten oxide synthesised by a templated sol-gel process from tungstic acid precursor," *Microporous and Mesoporous Materials*, vol. 121, no. 1–3, pp. 121–128, 2009.
- [20] N. O. Balayeva, M. Fleisch, and D. W. Bahnemann, "Surface-grafted WO_3/TiO_2 photocatalysts: Enhanced visible-light activity towards indoor air purification," *Catalysis Today*, vol. 313, pp. 63–71, 2018.
- [21] L. Rimoldi, A. Giordana, G. Cerrato, E. Falletta, and D. Meroni, "Insights on the photocatalytic degradation processes supported by TiO_2/WO_3 systems. The case of ethanol and tetracycline," *Catalysis Today*, vol. 328, pp. 210–215, 2019.
- [22] E. Bárdos, G. Kovács, T. Gyulavári et al., "Novel synthesis approaches for WO_3 - TiO_2 /MWCNT composite photocatalysts- problematic issues of photoactivity enhancement factors," *Catalysis Today*, vol. 300, pp. 28–38, 2018.
- [23] L. Keith and W. Telliard, "ES&T special report: priority pollutants: I-a perspective view," *Environmental Science & Technology*, vol. 13, no. 4, pp. 416–423, 1979.

- [24] J. Mejjide, E. Rosales, M. Pazos, and M. A. Sanromán, "*p*-Nitrophenol degradation by electro-Fenton process: pathway, kinetic model and optimization using central composite design," *Chemosphere*, vol. 185, pp. 726–736, 2017.
- [25] K. Qian, W. Huang, Z. Jiang, and H. Sun, "Anchoring highly active gold nanoparticles on SiO₂ by CoOx additive," *Journal of Catalysis*, vol. 248, no. 1, pp. 137–141, 2007.
- [26] Saepurahman, M. A. Abdullah, and F. K. Chong, "Preparation and characterization of tungsten-loaded titanium dioxide photocatalyst for enhanced dye degradation," *Journal of Hazardous Materials*, vol. 176, no. 1-3, pp. 451–458, 2010.
- [27] A. K. L. Sajjad, S. Shamaila, B. Tian, F. Chen, and J. Zhang, "One step activation of WO_x/TiO₂ nanocomposites with enhanced photocatalytic activity," *Applied Catalysis B: Environmental*, vol. 91, no. 1-2, pp. 397–405, 2009.
- [28] S. A. K. Leghari, S. Sajjad, F. Chen, and J. Zhang, "WO₃/TiO₂ composite with morphology change via hydrothermal template-free route as an efficient visible light photocatalyst," *Chemical Engineering Journal*, vol. 166, no. 3, pp. 906–915, 2011.
- [29] E. Luévano-Hipólito, A. Martínez-de la Cruz, E. López-Cuellar, Q. L. Yu, and H. J. H. Brouwers, "Synthesis, characterization and photocatalytic activity of WO₃/TiO₂ for NO removal under UV and visible light irradiation," *Materials Chemistry and Physics*, vol. 148, no. 1-2, pp. 208–213, 2014.
- [30] J. Tauc, "Optical properties and electronic structure of amorphous Ge and Si," *Materials Research Bulletin*, vol. 3, no. 1, pp. 37–46, 1968.
- [31] Z. D. Meng, L. Zhu, J. G. Choi, C. Y. Park, and W. C. Oh, "Preparation, characterization and photocatalytic behavior of WO₃-fullerene/TiO₂ catalysts under visible light," *Nanoscale Research Letters*, vol. 6, no. 1, pp. 459–470, 2011.
- [32] W. Chen, C. Takai, H. R. Khosroshahi, M. Fuji, and T. Shirai, "SiO₂/TiO₂ double-shell hollow particles: fabrication and UV-Vis spectrum characterization," *Advanced Powder Technology*, vol. 27, no. 3, pp. 812–818, 2016.
- [33] H. Y. Song, H. F. Jiang, X. Q. Liu, Y. Z. Jiang, and G. Y. Meng, "Preparation of WO_x-TiO₂ and the photocatalytic activity under visible irradiation," *Key Engineering Materials*, vol. 336-338, pp. 1979–1982, 2007.
- [34] J. L. Rodríguez, T. Poznyak, M. A. Valenzuela, H. Tiznado, and I. Chairez, "Surface interactions and mechanistic studies of 2,4-dichlorophenoxyacetic acid degradation by catalytic ozonation in presence of Ni/TiO₂," *Chemical Engineering Journal*, vol. 222, pp. 426–434, 2013.
- [35] T. F. Chala, C. M. Wu, M. H. Chou, M. B. Gebeyehu, and K. B. Cheng, "Highly efficient near infrared photo-thermal conversion properties of reduced tungsten oxide/polyurethane nanocomposites," *Nanomaterials*, vol. 7, no. 7, p. 191, 2017.
- [36] P. N. Kuznetsov, A. V. Obukhova, L. I. Kuznetsova, and Y. L. Mikhlin, "Dynamics of the activity and physicochemical characteristics of Pt/WO₄²⁻-ZrO₂ catalysts in the hydroisomerization of heptane and heptane-benzene mixtures," *Catalysis Letters*, vol. 147, no. 3, pp. 773–784, 2017.
- [37] P. H. Wu, X. Y. Yu, C. W. Cheng, C. H. Liao, S. W. Feng, and H. C. Wang, "Ultrafast ablation dynamics in fused silica with a white light beam probe," *Optics Express*, vol. 19, no. 17, pp. 16390–16400, 2011.
- [38] B. Ma, J. Kim, T. Wang et al., "Improvement of photocatalytic oxidation activity on a WO₃/TiO₂ heterojunction composite photocatalyst with broad spectral response," *RSC Advances*, vol. 5, no. 97, pp. 79815–79819, 2015.
- [39] S. Collado, A. Laca, and M. Díaz, "Effect of the carboxylic substituent on the reactivity of the aromatic ring during the wet oxidation of phenolic acids," *Chemical Engineering Journal*, vol. 166, no. 3, pp. 940–946, 2011.
- [40] T. Wang, G. Qu, Q. Sun, D. Liang, and S. Hu, "Evaluation of the potential of *p*-nitrophenol degradation in dredged sediment by pulsed discharge plasma," *Water Research*, vol. 84, pp. 18–24, 2015.